OG-TPTV: A Texture-Preserving Regularizer for Hyperspectral Image Denoising

Zhangping Wu[1], Mi Wang[1]

[1] State Key Laboratory of Information Engineering in Surveying, Mapping and Remote Sensing, Wuhan University, Wuhan 430079, China - (wuzp2318, wangmi)@whu.edu.cn

Keywords: Hyperspectral image (HSI), Mixed noise, Denoising, Outlier-guided, Spatial representation coefficients (SRCs).

Abstract

Hyperspectral images (HSIs) are often severely degraded by mixed noise, such as Gaussian, stripe, and impulse noise during acquisition and transmission, which seriously impedes their subsequent applications. Therefore, HSI denoising is both crucial and challenging. In this work, we present a gradient-domain outlier-guided texture-preserved total variation (OG-TPTV) regularizer designed to remove mixed noise in HSIs. First, we utilize the mode-3 low-rank property of HSI gradient maps along the spectral dimension and apply a low-rank decomposition model to extract their spatial representation coefficients (SRCs). To improve the sparsity characterization of SRCs in the gradient subspace, an outlier-guided strategy is introduced. Specifically, we perform outlier detection on gradient maps to distinguish noise from texture structures and remove outliers to generate precise texture weighting maps. The resulting texture weight maps offer adaptive guidance for adjusting the strength of the sparsity constraints. Finally, a denoising method for HSIs is developed based on OG-TPTV. Extensive experiments on both synthetic and real HSIs demonstrate the superior denoising performance of our method.

1. Introduction

High-quality hyperspectral images (HSIs) are widely used in various applications, such as land cover classification (Zhao et al., 2016), environmental monitoring (Sun et al., 2021), spectral unmixing (Yao et al., 2019), and anomaly detection (Fu et al., 2021), due to their rich spatial-spectral characteristics. However, HSIs are often corrupted by mixed noise, including Gaussian, impulse, stripe noise, and deadlines, due to factors like sensor malfunctions, atmospheric interference, and photon effects (Liu et al., 2023), which significantly degrade data quality. Therefore, removing mixed noise from HSIs effectively remains a critical and challenging task.

HSI denoising methods can be broadly categorized into two groups: deep learning (DL)-based methods and prior model-based methods (Zhang et al., 2024). DL-based methods typically rely on paired clean–noisy data to learn the mapping from noisy inputs to clean outputs using various network architectures (Li et al., 2023). However, these supervised methods often face limited generalization due to their reliance on specific training data. In contrast, unsupervised learning methods leverage the intrinsic properties of HSI data to enhance generalization (Shi et al., 2024) . Although these methods eliminate the need for paired training samples, they still encounter challenges in interpretability and computational complexity.

Priors extensively mined for prior model-based methods include local smoothness priors and low-rank priors (Liu et al., 2025). The total variation (TV) model is a classical method based on the local smoothness prior. To fully leverage both spectral and spatial structural information, the spectral–spatial adaptive hybrid TV (SSAHTV) model was introduced, which adaptively adjusts the denoising strength (Yuan et al., 2012). To better preserve image texture structures, the adaptive spectral–spatial total variation (ASSTV) model was developed, which estimates gradient weights along each dimension (Chen et al., 2022). In recent years, the subspace representation-based methods have gained popularity for HSI denoising due to their ability to significantly reduce computational complexity. Consequently, increasing attention has been paid to modeling spatial representation coefficients (SRCs) (Yang et al., 2025). The representative coefficient TV (RCTV) model applies TV regularization to SRCs of HSIs, significantly improving denoising efficiency (Peng et al., 2022). Additionally, spectral correlations observed in the original HSIs are also present in gradient maps, leading to the development of the enhanced 3-D TV (E-3DTV) model, which applies TV regularization to SRCs of gradient maps (Peng et al., 2020). Due to the inherent spectral and spatial low-rank property of HSIs, low-rank prior models based on matrices or tensors have been widely adopted. Matrix-based low-rank priors unfold HSI data along the spectral dimension into 2-D matrices, followed by low-rank modeling. Representative methods include LRMR (Zhang et al., 2013) and NAILRMA (He et al., 2015). However, these methods inevitably disrupt the original spatial structure of HSIs, as they require reshaping the 3-D data into 2-D matrices for low-rank modeling. As a result, some approaches treat HSIs as 3-D tensors to preserve their inherent 3-D structure and the spatial–spectral structural correlations. Representative methods mainly rely on low-rank tensor decomposition (Zhou et al., 2024) and tensor nuclear norms (TNNs) (Fan et al., 2017).

In this work, we introduce a novel outlier-guided texture-preserved total variation (OG-TPTV) regularizer in the gradient domain for HSI denoising. The main contributions of this work are summarized as follows:

1. To characterize the sparsity of SRCs in the gradient subspace, we introduce the OG-TPTV regularizer. An outlier-guided strategy is applied, where outlier detection and removal are used to generate texture weight maps that adaptively guide the sparsity constraint strength, preserving fine-grained texture structures.
2. Based on the proposed OG-TPTV regularizer, we formulate a new HSI denoising model and develop an efficient optimization algorithm using the alternating direction method of multipliers (ADMM).

This contribution has been peer-reviewed. The double-blind peer-review was conducted on the basis of the full paper.
https://doi.org/10.5194/isprs-annals-XI-3-2026-325-2026

2. Preliminaries

2.1 Notations

For a given HSI $\mathcal{X} \in \mathbb{R}^{M\times N\times B}$, where M, N, and B denote the spatial height, width, and the number of spectral bands, respectively, its unfolding matrix along the spectral mode is denoted as $\mathbf{X} = \text{unfold}(\mathcal{X}) \in \mathbb{R}^{MN\times B}$ and $\mathcal{X} = \text{fold}(\mathbf{X}) \in \mathbb{R}^{M\times N\times B}$, where fold is the inverse of unfolding operator. We also denote the difference operation along the i-th mode of $\mathcal{X}$ as D_i, where $i = 1, 2, 3$ corresponds to the spatial height, spatial width, and spectral mode, respectively. Specifically:

$$\mathcal{G}_i = D_i(X), \quad \forall i = 1, 2, 3. \tag{1}$$

where $\mathcal{G}_i \in \mathbb{R}^{M\times N\times B}$ denotes the gradient-map tensor of $\mathcal{X}$ along the i-th mode. Then, we denote the unfolding matrices of the gradient maps along the spectral mode as:

$$\mathbf{G}_i = \text{unfold}(\mathcal{G}_i), \quad \forall i = 1, 2, 3. \tag{2}$$

According to (Peng et al., 2020), all three operations are linear. We therefore denote the following three linear operators:

$$\nabla_i \mathbf{X} = \text{unfold}\left(D_i\left(\text{fold}(\mathbf{X})\right)\right) = \mathbf{G}_i, \quad \forall i = 1, 2, 3. \tag{3}$$

where ∇_i denotes special difference operation on the matrix.

2.2 Outlier Identification and Elimination Using the Grubbs Criterion

The Grubbs criterion is a classical method for detecting and eliminating outliers, applicable under the assumption that the data follow a Gaussian distribution. Unlike many other approaches, the Grubbs test does not require prior knowledge of the sample mean or variance, making it both flexible and easy to apply (Shen et al., 1999). Given a set of observed samples $y_i, i = 1, 2, \ldots, P$, the observation model is defined as:

$$y_i = \mu + x_i, x_i \sim N\left(0, \sigma^2\right) \tag{4}$$

The sample mean $\bar{y}$ and standard deviation $\hat{\sigma}$ are calculated as follows:

$$\bar{y} = \frac{1}{P}\sum_{i=1}^{P} y_i, \quad \hat{\sigma} = \sqrt{\frac{1}{P-1}\sum_{i=1}^{P}(y_i - \bar{y})^2} \tag{5}$$

Following the approach in (Shen et al., 1999), the test statistic v is defined as follows:

$$v = \max_{1\le i\le P} |y_i - \bar{y}| \tag{6}$$

Outlier detection is performed using Grubbs criterion as follows:

$$v \ge g(P, \alpha/2)\hat{\sigma} \tag{7}$$

Here, α denotes the significance level, and $g(P, \alpha/2)$ is the critical value, which depends only on the sample size P and the selected significance level α. If condition (7) is satisfied, the sample corresponding to the statistic v is identified as an outlier and removed. The sample size is then reduced by one, and the procedure is iteratively repeated until no additional outliers are detected.

3. Proposed Method

3.1 Outlier-Guided Texture-Preserved Total Variation (OG-TPTV)

The 3DTV (Wang et al., 2018) characterizes the local smoothness prior of HSI and is defined as

$$\|\mathbf{X}\|_{\text{3DTV}} = \sum_{i=1}^{3} \|\mathbf{G}_i\|_1 \tag{8}$$

Although 3DTV has been widely applied in HSI processing, it assumes that the sparsity of gradient maps across all spectral bands is identical and independent, which conflicts with real HSI spectral characteristics (Peng et al., 2020). To address this limitation, the Laplacian scale mixture (LSM) model is employed to characterize the distribution of gradient maps, based on which a novel texture-preserved total variation regularizer (TPTV) is developed (Chen et al., 2023):

$$\|\mathcal{Z}\|_{\text{TPTV}} = \|D_1\mathcal{Z}\|_{W_1,1} + \|D_2\mathcal{Z}\|_{W_2,1} + \|D_3\mathcal{Z}\|_{W_3,1} \tag{9}$$

By introducing weighting coefficients W_i, TPTV can impose varying degrees of sparsity constraints on flat and edge regions, thereby effectively preserving image texture structures. Intuitively, W_i should be negatively correlated with the local texture intensity: pixels with rich textures should be assigned smaller weights to relax the sparsity constraint, while those in homogeneous regions should receive larger weights to enforce stronger sparsity. Consequently, a reliable texture map is essential.

Inspired by (Chen et al., 2023), the gradient maps of clean HSIs effectively capture texture information. However, clean HSIs are typically unavailable in practical scenarios. To mitigate this, we incorporate low-rank filtering into the denoising process to further suppress noise. However, in the early stages of denoising, the noise level remains relatively high. Residual noise after low-rank filtering may still disrupt texture structures in the gradient maps, thereby hindering the accurate extraction of texture maps. To address this issue, we exploit the structural consistency of HSI textures and the random nature of noise, and propose applying the Grubbs criterion to the gradient maps for further noise suppression. The specific procedure is as follows: During the denoising process, low-rank filtering is applied to the recovered HSI $\hat{\mathbf{X}}$:

$$\mathbf{X_0} = \text{F}(\hat{\mathbf{X}}) \tag{10}$$

Here, $\text{F}(\cdot)$ denotes the low-rank filtering operator. Since the noise level is high in the initial stages of denoising, the rank is initially set to 1. As denoising proceeds and noise is progressively reduced, the rank is gradually increased. Although gradient maps $\nabla_i\mathbf{X_0}$ can capture texture information, residual noise may still degrade fine texture details. To further suppress residual noise, it is treated as outliers and is detected and removed using the Grubbs criterion, ultimately producing higher-quality texture maps. The corresponding formulation is as follows:

$$T_i = \text{GM}(\nabla_i\mathbf{X_0}), \quad i = 1, 2, 3. \tag{11}$$

Here, T_i denotes the texture map along the i-th dimension, $\text{GM}(\cdot)$ indicates the sample mean computed after outlier removal via the Grubbs criterion.

Algorithm 1 The OG-TPTV for HSI Denoising Algorithm

Input: Noisy HSI $\mathcal{Y} \in \mathbb{R}^{M\times N\times B}$, unfolding to the matrix $\mathbf{Y} \in \mathbb{R}^{MN\times B}$, parameter β, threshold γ, significance level α, stopping criterion ξ and maximum number of iterations k_{max}.
Output: Denoised HSI $\mathrm{Fold}(\mathbf{X}) \in \mathbb{R}^{M\times N\times B}$.

Initialize: $\mathbf{X}^0 = \mathbf{Y}$, $\mathbf{L}_1 = \mathbf{L}_2 = \mathbf{L}_2 = \mathbf{L}_4 = \mathbf{0}$, $\alpha = 0.05$, $\mu = 10^{-2}$, $\mu_{max} = 10^6$, $\rho = 1.2$, $\xi = 10^{-6}$, and $k_{max} = 60$
for $k = 1 : k_{max}$ **do**
  Update $\mathbf{S}$ by (19);
  Update $\mathbf{U}_i$ and $\mathbf{V}_i$ by (22) and (24);
  Update $\mathbf{X}$ by (27);
  Update $W_i, i = 1, 2, 3$ by (28);
  Update Lagrange multipliers $\mathbf{L}_i, i = 1, 2, 3, 4$ and the penalty parameter μ by (29);
  Check convergence $\left\|\mathbf{X}^{k+1} - \mathbf{X}^k\right\|_F / \left\|\mathbf{X}^k\right\|_F \le \xi$
end for

Subsequently, the weight coefficients W_i are computed from the texture maps T_i as follows:

$$W_i = \frac{\max\left(|T_i|\right)}{|T_i| + \gamma \max\left(|T_i|\right)} \tag{12}$$

Here, γ denotes the threshold adopted to control the range of weight values, usually set to the first quartile of normalized $|T_i|$.

Due to the fact that the gradient maps of HSIs also possess low-rank properties (Peng et al., 2020), expressed as follows:

$$\mathbf{G}_i = \mathbf{U}_i\mathbf{V}_i^T, \quad \mathbf{V}_i^T\mathbf{V}_i = I, \quad i = 1, 2, 3. \tag{13}$$

where $\mathbf{U}_i \in \mathbb{R}^{MN\times r}$ and $V_i \in \mathbb{R}^{B\times r}$ represent the SRCs and spectral basis, respectively, and r is the rank of $\mathcal{X}$ along the spectral mode. Since $\mathbf{U}_i$ exhibits a clearer and more noise-robust sparse prior structure, We apply the OG-TPTV regularizer to $\mathbf{U}_i$, defined as:

$$\begin{aligned}\|\mathbf{X}\|_{\text{OG-TPTV}} = &\sum_{i=1}^{3} \min_{\mathbf{U}_i,\mathbf{V}_i} \|\mathbf{U}_i\|_{W_i,1} \\ &\text{s.t. } \nabla_i\mathbf{X} = \mathbf{U}_i\mathbf{V}_i^T, \mathbf{V}_i^T\mathbf{V}_i = I, \\ &\quad i = 1, 2, 3\end{aligned} \tag{14}$$

3.2 Model Optimization

We assume that the noise is additive, and the observation model can be formulated as follows:

$$\mathbf{Y} = \mathbf{X} + \mathbf{S} \tag{15}$$

In this model, $\mathbf{Y}$ denotes the noise-corrupted HSI, $\mathbf{X}$ represents the underlying clean HSI, and $\mathbf{S}$ stands for sparse noise. Based on this, the proposed HSI denoising model is formulated as:

$$\begin{aligned}&\min_{\mathbf{X},\mathbf{S},\mathbf{U_i},\mathbf{V}_i} \beta\sum_{i=1}^{3} \|\mathbf{U}_i\|_{W_i,1} + \|\mathbf{S}\|_1 \\ &\text{s.t. } \mathbf{Y} = \mathbf{X} + \mathbf{S}, \\ &\quad \nabla_i\mathbf{X} = \mathbf{U}_i\mathbf{V}_i^T, \mathbf{V}_i^T\mathbf{V}_i = I, \quad i = 1, 2, 3\end{aligned} \tag{16}$$

β is a parameter that balances the OG-TPTV regularization term and the sparse noise component. The optimization problem in (16) can be efficiently solved by ADMM algorithm.

The augmented Lagrangian function of (16) can be expressed as follows:

$$\begin{aligned}&L(\mathbf{X}, \mathbf{S}, \mathbf{U}_i, V_i, \mathbf{L}_i) \\ &= \beta\sum_{i=1}^{3} \|\mathbf{U}_i\|_{W_i,1} + \|\mathbf{S}\|_1 \\ &\quad + \mu\sum_{i=1}^{3} \left\|\nabla_i\mathbf{X} - \mathbf{U}_i\mathbf{V}_i^T + \frac{\mathbf{L}_{i+1}}{\mu}\right\|_F^2 \\ &\quad + \mu\left\|\mathbf{Y} - \mathbf{X} - \mathbf{S} + \frac{\mathbf{L}_1}{\mu}\right\|_F^2\end{aligned} \tag{17}$$

Here, $\mathbf{L}_i, i = 1, 2, 3, 4$ denotes the Lagrange multipliers, μ is the penalty parameter. (17) can be solved by minimizing each variable alternately while keeping the others fixed.

1. **Updating S:** The subproblem with respect to $\mathbf{S}$ can be expressed as:

$$\min_{\mathbf{S}} \|\mathbf{S}\|_1 + \mu\left\|\mathbf{Y} - \mathbf{X} + \frac{1}{\mu}\mathbf{L}_1 - \mathbf{S}\right\|_F^2 \tag{18}$$

The computation is performed using the soft-shrinkage operator as follows:

$$\mathbf{S}^{k+1} = \mathrm{shrink}_{\frac{1}{\mu}}\left(\mathbf{Y} - \mathbf{X} + \frac{1}{\mu}\mathbf{L}_1\right) \tag{19}$$

where shrink denotes the soft-shrinkage operator:

$$\mathrm{shrink}(r, \xi) = \max(r - \xi, 0) * \frac{r}{|r|} \tag{20}$$

2. **Updating $\mathbf{U}_i$ and $\mathbf{V}_i$:** Based on (Chen et al., 2023), we first update the spectral subspace basis $\mathbf{V}_i$ by solving a low-rank matrix decomposition problem as follows:

$$\min_{\mathbf{U}_i,\mathbf{V}_i} \left\|\nabla_i\mathbf{X} - \mathbf{U}_i\mathbf{V}_i^T + \frac{1}{\mu}\mathbf{L}_{i+1}\right\|_F^2 \tag{21}$$

$\mathbf{V}_i$ can be obtained by singular value decomposition (SVD) as follows:

$$\left\{\mathbf{U}_i^{k+\frac{1}{2}}, \mathbf{V}_i^{k+1}\right\} = \mathrm{svd}\left(\nabla_i\mathbf{X} + \frac{1}{\mu}\mathbf{L}_i\right) \tag{22}$$

Then, $\mathbf{U}_i^{k+\frac{1}{2}}$ is projected onto the sparse space as follows:

$$\min_{\mathbf{U}} \left\|\mathbf{U}_i^{k+\frac{1}{2}} - \mathbf{U}\right\|_F^2 + \frac{\beta}{\mu}\|\mathbf{U}_i\|_{W_i,1} \tag{23}$$

Similarly, using the soft-shrinkage operator we can obtain:

$$\mathbf{U}_i^{k+1} = \mathrm{shrink}_{\frac{\beta W_i}{\mu}}\left(\mathbf{U}_i^{k+\frac{1}{2}}\right) \tag{24}$$

3. **Updating X:** The subproblem with respect to $\mathbf{X}$ can be expressed as:

$$\begin{aligned}\min_{\mathbf{X}} &\left\|\mathbf{Y} - \mathbf{S} + \frac{\mathbf{L}_1}{\mu} - \mathbf{X}\right\|_F^2 \\ &+ \sum_{i=1}^{3} \left\|\mathbf{U}_i\mathbf{V}_i^T - \frac{\mathbf{L}_{i+1}}{\mu} - \nabla_i\mathbf{X}\right\|_F^2\end{aligned} \tag{25}$$

(25) is a quadratic minimization problem and can be solved by the following linear system:

$$\left(\sum_{i=1}^{3}\nabla_i^*\nabla_i+\mathbf{I}\right)\mathbf{X}=\sum_{i=1}^{3}\nabla_i^*\left(\mathbf{U}_i\mathbf{V}_i^T-\frac{\mathbf{L}_{i+1}}{\mu}\right)+\left(\mathbf{Y}-\mathbf{S}+\frac{\mathbf{L}_1}{\mu}\right) \tag{26}$$

Here, ∇_i^* denotes the adjoint operator of ∇_i. The problem is solved using the fast Fourier transform (FFT) as follows:

$$\mathbf{X}^{k+1}=\mathrm{ifftn}\left(\frac{\mathrm{fftn}(\mathbf{H})}{\mathbf{1}+\mathbf{J}}\right) \tag{27}$$

where $\mathbf{H}=\mathbf{Y}-\mathbf{S}+\frac{\mathbf{L}_1}{\mu}+\sum_{i=1}^{3}\nabla_i^*\left(\mathbf{U}_i\mathbf{V}_i^T-\frac{\mathbf{L}_{i+1}}{\mu}\right)$ and $\mathbf{J}=|\,\mathrm{fftn}(\nabla_1)|^2+|\,\mathrm{fftn}(\nabla_2)|^2+|\,\mathrm{fftn}(\nabla_3)|^2$. fftn and ifftn are the fast 3-D Fourier transform and its inverse transform, $\mathbf{1}$ is a tensor with the same size as $\mathbf{J}$ and all of the elements are 1.

4. **Updating W_i:** Based on $\mathbf{X}^{k+1}$, texture maps T_i and weight coefficient W_i are updated synchronously as follows:

$$\begin{cases}\mathbf{X}_L=\mathrm{F}(\mathbf{X}^{k+1})\\ T_i=\mathrm{GM}(\nabla_i\mathbf{X}_L)\\ W_i=\frac{\max(|T_i|)}{|T_i|+\gamma\max(|T_i|)},\quad i=1,2,3\end{cases} \tag{28}$$

where $\mathbf{X}_L$ represents the result of applying low-rank filtering to $\mathbf{X}^{k+1}$.

5. **Updating $\mathbf{L}_i, i=1,2,3,4$ and μ:** The Lagrange multipliers $\mathbf{L}_i, i=1,2,3,4$ and penalty parameter μ are updated as follows:

$$\begin{cases}\mathbf{L}_1^{k+1}=\mathbf{L}_1^k+\mu(\mathbf{Y}-\mathbf{X}-\mathbf{S})\\ \mathbf{L}_i^{k+1}=\mathbf{L}_i^k+\mu\left(\nabla_i\mathbf{X}-\mathbf{U}_i\mathbf{V}_i^T\right),\quad i=2,3,4\\ \mu=\min(\mu_{max},\rho\mu)\end{cases} \tag{29}$$

where $\rho>1$ denotes constant values.

Moreover, the concise description of the proposed algorithm is summarized in Algorithm 1.

4. Experiments and Analysis

To evaluate the effectiveness of the proposed method, extensive experiments were conducted on both synthetic and real datasets. Seven advanced HSI denoising methods were selected for comparison, including NGMeet (He et al., 2022), BALMF (Xu et al., 2022), WNLRATV (Chen et al., 2022), RCTV (Peng et al., 2022), LRTDTV (Wang et al., 2018), FastHyMix (Zhuang and Ng, 2023), and RCILD (Peng et al., 2024). The evaluation metrics included mean peak signal-to-noise ratio (MPSNR), mean structural similarity index (MSSIM), spectral angle mapper (SAM), and the Erreur Relative Globale Adimensionnellede Synthese (ERGAS). Higher MPSNR/MSSIM and lower SAM/ERGAS indicate superior denoising quality. The parameters for all comparison methods were tuned according to the settings recommended in their original publications. Moreover, the pixel values of each band were normalized to [0, 1].

4.1 Simulated Experiments

Simulation experiments were conducted on two HSI datasets: Pavia University (PaviaU) and Washington DC Mall (WDC). The subimage sizes for PaviaU and WDC are $300\times300\times87$ and $200\times200\times191$, respectively. Four types of noise were considered in the experiments:

1. Case 1 (Gaussian Non-i.i.d. Noise): Non-i.i.d. Gaussian noise with standard deviation ranging from 5 to 30 was added to each band.

2. Case 2 (Gaussian + Impulse Noise): Gaussian noise (as in Case 1) and impulse Noise. The impulse noise density ranged from 0.05 to 0.3, and 30% of bands were randomly selected for impulse noise injection.

3. Case 3 (Gaussian + Stripe Noise): Gaussian noise (as in Case 1) and stripe Noise. 30% of bands were randomly selected to add stripe noise with the stripe ratio in [0.05, 0.3].

4. Case 4 (Gaussian Noise + Stripes + Impulse Noise): A mixture of Gaussian noise (as in Case 1), impulse noise (as in Case 2), and stripe noise (as in Case 3) was added to the images.

The quantitative metrics of different methods are listed in Table 1, with the best values for each metric highlighted in bold. As observed from the table, the proposed method achieves superior metric values in most cases. Fig. 1 shows the visual denoising results. In Case 4, RCILD and FastHyMix fail to effectively remove stripe noise, while LRTDTV and BALMF leave noticeable residual noise. NGMeet and WNLRATV tend to over-smooth fine image details. In contrast, our method demonstrates superior capability in handling various types of mixed noise, maintaining excellent performance in preserving spatial details and spectral consistency.

Fig. 2 shows the spectral curves of the recovered HSI compared with the original HSI. The red curve represents the original spectrum, while the green curves represent those restored by different methods. The proposed method provides the best fit to the original spectral curve, further validating its superiority in preserving spectral information.

We further analyzed the mean cross-track profile curves of denoised results obtained using different methods. The results are shown in Fig. 3, where the top represents the 115th band of the WDC dataset under Case 4, and the bottom represents the 34th band of the PaviaU dataset under Case 4. The red curve represents the mean cross-track profile of the clean HSI, while the green curves represent the noisy HSI or the results denoised by different methods. The curve obtained by the proposed method is closer to that of the clean HSI, indicating better preservation of spatial details.

Fig. 4 presents the PSNR and SSIM curves obtained by different methods under Case 4 for the WDC and PaviaU datasets. Specifically, (a) and (b) show the PSNR and SSIM curves for the WDC dataset, while (c) and (d) show those for the PaviaU dataset. Most methods exhibit significant fluctuations in their PSNR and SSIM curves, especially in spectral bands affected by stripe noise. In contrast, the proposed method produces smoother curves and consistently achieves higher and more stable PSNR and SSIM values across most bands, demonstrating its robustness and effectiveness.

Dataset	Method	Case 1				Case 2				Case 3				Case 4			
		MPSNR	MSSIM	ERGAS	SAM	MPSNR	MSSIM	ERGAS	SAM	MPSNR	MSSIM	ERGAS	SAM	MPSNR	MSSIM	ERGAS	SAM
PaviaU	**NGMeet**	36.04	0.909	84.98	7.15	30.08	0.862	241.53	13.34	35.58	0.908	93.77	7.12	29.55	0.849	259.12	13.77
	BALMF	36.35	0.924	72.06	5.7	34.12	0.89	143.54	10.11	35.65	0.908	79.76	6.07	33.21	0.881	162.19	10.02
	WNLRATV	39.29	0.964	49.29	3.89	38.32	0.951	186.18	7.93	38.29	0.955	58.01	4.25	37.75	0.948	185.28	7.96
	RCTV	38.28	0.969	48.43	2.95	37.94	**0.967**	50.61	2.98	37.68	**0.965**	52.37	3.12	37.33	**0.962**	54.2	3.14
	LRTDTV	36.59	0.935	65.09	5.01	29.69	0.807	265.23	16.12	35.66	0.922	78.81	5.82	29.22	0.8	264.84	16.01
	RCILD	**39.72**	**0.972**	45.03	3.33	34.65	0.927	169.58	11.56	36.63	0.932	107.97	6.68	34.19	0.924	141.35	10.15
	FastHyMix	39.49	0.971	47.72	3.52	37.15	0.956	128.97	9.82	37.72	0.935	67.42	5.17	36.08	0.926	111.02	8.88
	Proposed	39.44	0.97	**42.46**	**2.68**	**38.87**	0.966	**46.69**	**2.9**	**38.49**	0.964	**47.93**	**2.99**	**38.2**	0.961	**49.4**	**3.05**
WDC	**NGMeet**	34.64	0.818	331.73	4.75	29.37	0.734	650.27	10.54	33.22	0.786	379.5	5.62	28.77	0.718	959.42	11.73
	BALMF	38.79	0.933	103.15	2.45	36.83	0.889	133.59	3.72	38.17	0.923	108.48	2.65	37.15	0.894	125.07	3.55
	WNLRATV	37.63	0.892	110.97	2.66	37.76	0.911	109.11	2.73	36.97	0.885	115.29	3.02	37.33	0.9	107.95	2.86
	RCTV	39.9	0.969	62.91	2.46	39.67	0.965	64.41	2.59	39.63	0.966	64.52	2.53	39.39	0.964	66.77	2.67
	LRTDTV	33.84	0.807	309.85	4.32	28.97	0.711	793.3	11.23	32.53	0.777	372.75	5.27	28.46	0.695	1117.81	12.42
	RCILD	34.62	0.832	361.29	4.28	31.49	0.777	678.54	9.69	31.97	0.798	768.89	7.38	28.99	0.742	1040.3	12.6
	FastHyMix	35.98	0.826	375.87	4.09	33.87	0.812	491.23	7.33	34.25	0.805	382.63	4.92	33.21	0.803	469.63	7.67
	Proposed	**43.34**	**0.983**	**49.42**	**1.52**	**42.89**	**0.981**	**47.13**	**1.66**	**42.46**	**0.981**	**47.44**	**1.76**	**42.61**	**0.979**	**51.16**	**1.75**

Table 1. Quantitative comparison results on PaviaU and WDC datasets under four different noise cases.

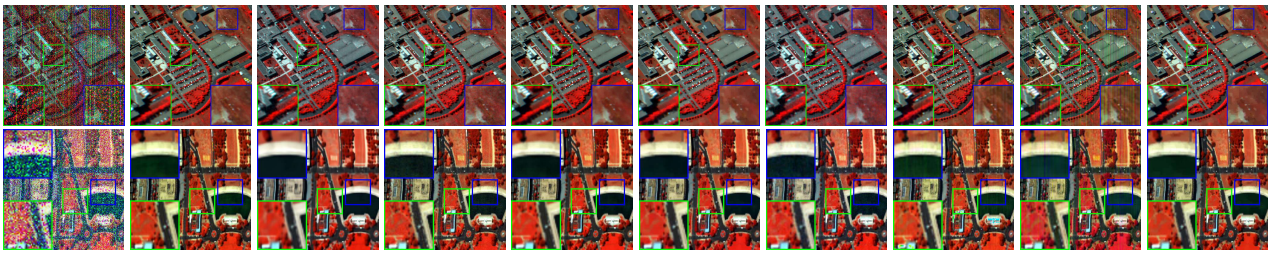

Figure 1. (Top) Denoising results for band (81, 34, 10) of the PaviaU dataset under Case 4. (Bottom) Band (58, 35, 16) of the WDC dataset under Case 4.

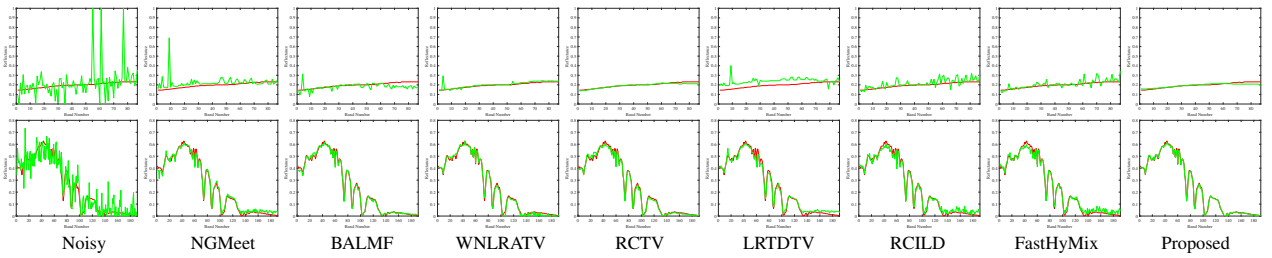

Figure 2. (Top) Original spectrum (red) and denoised results (green) for pixel (88, 88) under Case 4 of the PaviaU dataset. (Bottom) Original spectrum (red) and denoised results (green) for pixel (89, 25) under Case 3 of the WDC dataset.

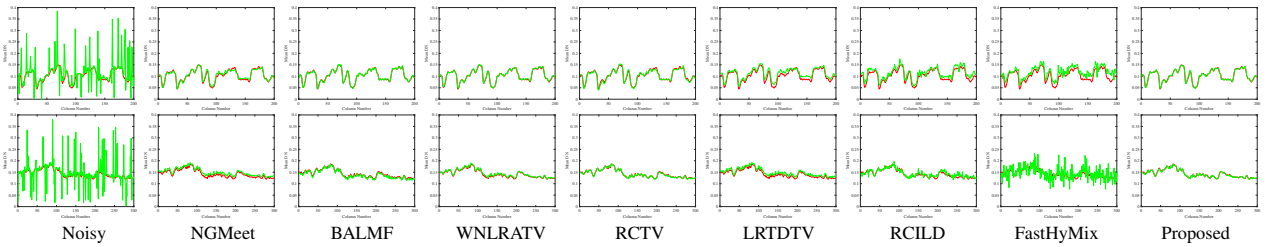

Figure 3. (Top) Original mean cross-track profile curves (red) and denoised results (green) for band 115 under Case 4 of the WDC dataset. (Bottom) Original mean cross-track profile curves (red) and denoised results (green) for band 34 under Case 4 of the PaviaU dataset.

This contribution has been peer-reviewed. The double-blind peer-review was conducted on the basis of the full paper.
https://doi.org/10.5194/isprs-annals-XI-3-2026-325-2026 | © Author(s) 2026. CC BY 4.0 License.

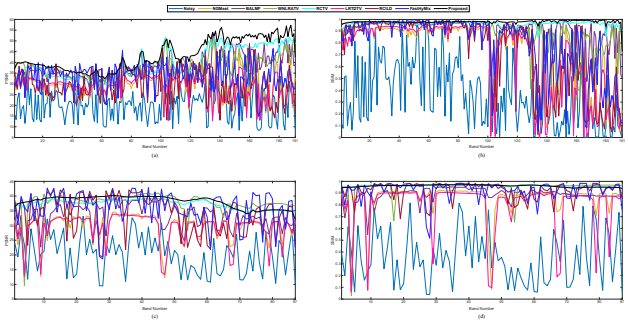

Figure 4. Overall PSNR and SSIM values for different methods under Case 4. (a) and (b) correspond to the WDC dataset, while (c) and (d) correspond to the PaviaU dataset.

Dataset	Method	Case 3				Case 4			
		MPSNR	MSSIM	ERGAS	SAM	MPSNR	MSSIM	ERGAS	SAM
PaviaU	w/o GM	38.27	0.962	53.72	3.43	37.96	0.96	54.98	3.67
	Proposed	**38.49**	**0.964**	**47.93**	**2.99**	**38.2**	**0.961**	**49.4**	**3.05**
WDC	w/o GM	42.24	0.978	58.93	1.79	42.1	0.976	79.85	1.89
	Proposed	**42.46**	**0.981**	**47.44**	**1.76**	**42.61**	**0.979**	**51.16**	**1.75**

Table 2. Quantitative results of ablation studies

4.2 Real Experiments

To further assess the performance of the proposed method, we conducted experiments on the real GF-5 Shanghai dataset. A subregion of size $300 \times 300 \times 155$ was extracted for evaluation.

Fig. 5 shows the pseudo-color image of the GF-5 Shanghai dataset, composed of the (38, 152, 155) bands. The original image is severely degraded by a mixture of stripe, Gaussian, and sparse noise. In the zoomed-in regions, noticeable stripe noise remains in the denoised results of NGMeet, BALMF, LRTDTV, and RCILD, while FastHyMix introduces visible artifacts. In contrast, WNLRATV, RCTV, and the proposed method provide the best visual performance.

Fig. 6 shows the mean cross-track profile curves of denoised results obtained by different methods on the GF-5 Shanghai dataset. The original GF-5 Shanghai image exhibits significant oscillations in its mean cross-track profile curve due to severe mixed noise, including stripe, Gaussian, and deadline noise. Most methods smooth the mean cross-track profile curve to some extent, although fluctuations remain at varying levels. In contrast, the mean cross-track profile curves obtained by WNLRATV and the proposed method show the best smoothing performance.

4.3 Ablation Study

To validate the effectiveness of the Grubbs criterion, we conducted an ablation study in which this component was disabled. Specifically, instead of applying the Grubbs criterion, we computed the texture images by performing mean filtering along the spectral dimension of the gradient maps. This variant is referred to as “w/o GM”. Table 2 presents the quantitative results of the ablation experiments on the PaviaU and WDC datasets under two noise cases. As shown, the proposed method consistently yields the best results, confirming the effectiveness of the Grubbs criterion in texture image estimation.

4.4 Classification Performance

To further evaluate the effectiveness of different denoising methods for downstream tasks, we conducted classification experiments on the real Indian Pines dataset, whose ground truth contains 16 land cover classes. In our experiments, support vector machine (SVM) was adopted as the classifier. Specifically, 10% of the labeled pixels were randomly selected for training, and the remaining pixels were used for testing.

Table 3 lists the classification metrics of different denoising methods, including overall accuracy (OA), average accuracy (AA), and kappa coefficient. The best results are highlighted in bold, while the second-best results are underlined. As can be observed, the proposed method achieves the highest OA and kappa values, along with the second-best AA performance. The corresponding classification maps are shown in Fig. 7. Overall, the proposed method achieves the best quantitative metrics and visual performance in the classification experiments, thereby verifying its effectiveness.

4.5 Algorithm Robustness

The robustness of OG-TPTV is evaluated through parameter sensitivity and numerical convergence. The parameters β and the ranks of the gradient maps along the three modes $r_i (i = 1, 2, 3)$ are critical parameters influencing the performance of the proposed model. As depicted in Fig. 8, the regularization parameter β effectively balances the trade-off between noise suppression and texture preservation; optimal performance is consistently achieved within $[0.6, 0.9]$. Beyond this range, the model either fails to suppress heavy mixed noise or suffers from over-smoothing. For the low-rank constraints, Fig. 9 reveals that the spatial rank r_1 is more decisive than the spectral rank r_2 in maintaining structural integrity, with both metrics remaining stable across $r_1, r_2 \in [4, 8]$. Furthermore, the convergence curves in Fig. 10 demonstrate that the relative change of the image component plunges significantly and plateaus within 50 iterations. This rapid and stable convergence validates the efficiency of the proposed optimization scheme in handling complex HSI degradation.

5. Discussion

The superior performance of OG-TPTV is rooted in its ability to decouple noise suppression from edge preservation. Unlike conventional TV regularizers that often produce ”staircase” artifacts by applying uniform sparsity priors, our outlier-guided strategy identifies gradient-domain anomalies—such as stripes and impulse spikes—prior to regularization. By adaptively relaxing constraints on true structural edges, the model ensures that the total variation penalty is precisely targeted at noise components, effectively retaining high-frequency textures that are typically suppressed in standard smoothing frameworks.

Quantitative evidence presented in Table 1 substantiates the superior performance of OG-TPTV. Notably, on the WDC dataset (Case 4), our method outperforms the most competitive baseline (RCTV) by a substantial margin of 3.22 dB in MPSNR and reduces the global error (ERGAS) by 23.4%. While MPSNR increments may appear numerically modest due to the logarithmic nature of the decibel scale, the dramatic 34.4% reduction in SAM manifests the model’s exceptional spectral fidelity. This discrepancy in metric sensitivity underscores that while spatial indices (MPSNR/MSSIM) verify structural recovery, spectral metrics like SAM better reflect the model’s capacity to mitigate spectral distortion during denoising—a critical factor often compromised in traditional TV-based frameworks.

This contribution has been peer-reviewed. The double-blind peer-review was conducted on the basis of the full paper.
https://doi.org/10.5194/isprs-annals-XI-3-2026-325-2026 | © Author(s) 2026. CC BY 4.0 License.

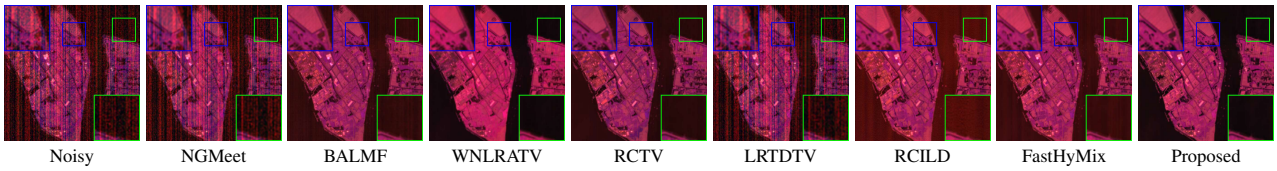

Figure 5. Restored results of different methods on band (38, 152, 155) of the GF-5 Shanghai image.

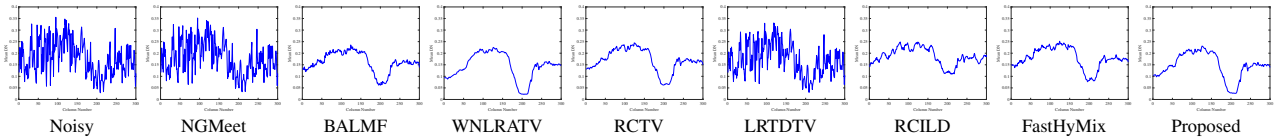

Figure 6. Mean cross-track profile curves of band 155 in the GF-5 Shanghai dataset.

Furthermore, ablation results in Table 2 confirm that the outlier-guided mechanism is indispensable, yielding an ERGAS reduction of up to 35.9% and proving that adaptive weighting is a prerequisite for robust HSI restoration under complex mixed noise.

The practical utility of OG-TPTV is further validated by the classification results in Table 3. Achieving the highest Overall Accuracy (0.6685) on the real Indian Pines dataset demonstrates that our denoising process successfully restores the discriminative spectral signatures necessary for material identification. This suggests that the proposed regularizer does not merely improve visual signal-to-noise ratios but preserves the intrinsic physical characteristics of the HSI cube, which is paramount for high-precision downstream applications.

6. Conclusion

In this paper, we presented a novel HSI regularization model, named OG-TPTV, designed to address HSI denoising. The OG-TPTV regularizer effectively captures both global spatial–spectral correlations and local smoothness by encoding the local smoothness of the SRCs in HSI gradient maps. Furthermore, we introduced an outlier-guided strategy to generate precise texture weighting maps, which dynamically adjust the sparsity constraint strength. Extensive experiments on both synthetic and real datasets demonstrate that the proposed method outperforms several state-of-the-art HSI denoising methods.

References

Chen, Y., Cao, W., Pang, L., Cao, X., 2022. Hyperspectral image denoising with weighted nonlocal low-rank model and adaptive total variation regularization. *IEEE Trans. Geosci. Remote Sens.*, 60. Art. no. 5544115.

Chen, Y., Cao, W., Pang, L., Peng, J., Cao, X., 2023. Hyperspectral image denoising via texture-preserved total variation regularizer. *IEEE Trans. Geosci. Remote Sens.*, 61. Art. no. 5516114.

Fan, H., Chen, Y., Guo, Y., Zhang, H., Kuang, G., 2017. Hyperspectral image restoration using low-rank tensor recovery. *IEEE J. Sel. Topcis Appl. Earth Observ. Remote Sens.*, 10(10), 4589–4604.

Fu, X., Jia, S., Zhuang, L., Xu, M., Zhou, J., Li, Q., 2021. Hyperspectral anomaly detection via deep plug-and-play denoising CNN regularization. *IEEE Trans. Geosci. Remote Sens.*, 59(11), 9553–9568.

He, W. et al., 2022. Non-local meets global: An iterative paradigm for hyperspectral image restoration. *IEEE Trans. Pattern Anal. Mach. Intell.*, 44(4), 2089–2107.

He, W., Zhang, H., Zhang, L., Shen, H., 2015. Hyperspectral image denoising via noise-adjusted iterative low-rank matrix approximation. *IEEE J. Sel. Topcis Appl. Earth Observ. Remote Sens.*, 8(6), 3050–3061.

Li, M., Liu, J., Fu, Y., Zhang, Y., Dou, D., 2023. Spectral enhanced rectangle transformer for hyperspectral image denoising. *Proc. IEEE Conf. Comput. Vis. Pattern Recognit. (CVPR))*, 5805–5814.

Liu, P., Long, H., Zheng, Z., Huang, N., Xiao, L., 2025. Gradient Subspace-Regularized Hyperspectral Image and Stripe-Coupled Non-convex Tensor Low-Rank Priors for Destriping and Denoising. *IEEE Trans. Geosci. Remote Sens.*, 63, 1–18. Art. no. 5507218.

Liu, T., Hu, D., Wang, Z., Gou, J., Chen, W., 2023. Hyperspectral image denoising using nonconvex fraction function. *IEEE Geosci. Remote Sens. Lett.*, 20, 1–5.

Peng, J. et al., 2024. Learnable representative coefficient image denoiser for hyperspectral image. *IEEE Trans. Geosci. Remote Sens.*, 62. Art. no. 5506516.

Peng, J., Wang, H., Cao, X., Liu, X., Rui, X., Meng, D., 2022. Fast noise removal in hyperspectral images via representative coefficient total variation. *IEEE Trans. Geosci. Remote Sens.*, 60. Art. no. 5546017.

Peng, J., Xie, Q., Zhao, Q., Wang, Y., Yee, L., Meng, D., 2020. Enhanced 3DTV regularization and its applications on HSI denoising and compressed sensing. *IEEE Trans. Image Process.*, 29, 7889–7903.

Shen, Y., Ran, Q., Liu, Y., 1999. Application of improved Grubbs’ criterion to estimation of signal detection threshold. *J. Harbin Inst. Technol.*, 31(3), 111–114.

Shi, K., Peng, J., Gao, J., Luo, Y., Xu, S., 2024. Hyperspectral Image denoising via Double Subspace Deep Prior. *IEEE Trans. Geosci. Remote Sens.*, 62. Art. no. 5531015.

Sun, W. et al., 2021. A simple and effective spectral-spatial method for mapping large-scale coastal wetlands using China ZY1-02D satellite hyperspectral images. *Int. J. Appl. Earth Observ. Geoinf.*, 104, 102572. Art. no. 102572.

Method	Noisy	NGMeet	BALMF	WNLRATV	RCTV	LRTDTV	RCILD	FastHyMix	Proposed
OA	0.6151	0.6086	0.5533	0.6200	0.4772	0.6650	0.5692	0.6540	**0.6685**
AA	0.7253	0.6980	0.6349	0.7254	0.5893	**0.7580**	0.7158	0.7450	0.7498
Kappa	0.5714	0.5641	0.5000	0.5771	0.4200	0.6247	0.5223	0.6125	**0.6281**

Table 3. Classification metrics of different methods on the real Indian Pines dataset.

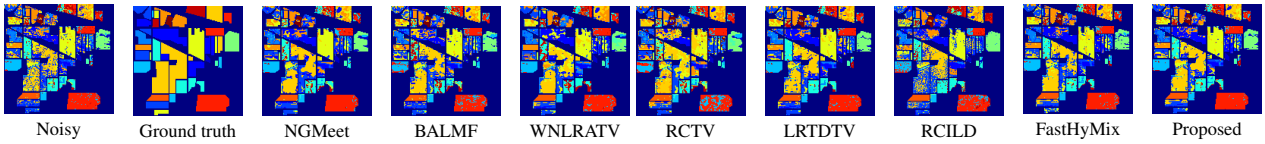

Figure 7. Classification maps of different methods on the real Indian Pines dataset.

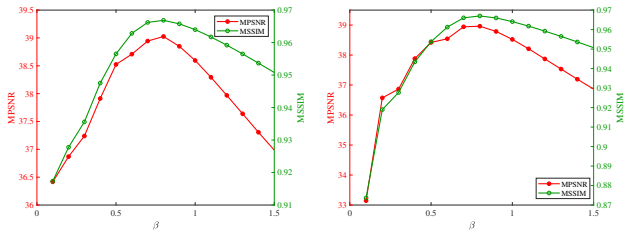

Figure 8. MPSNR and MSSIM change versus parameter β with $r_1 = 6$ and $r_2 = 4$ on the PaviaU dataset. (a) Case3. (b) Case4.

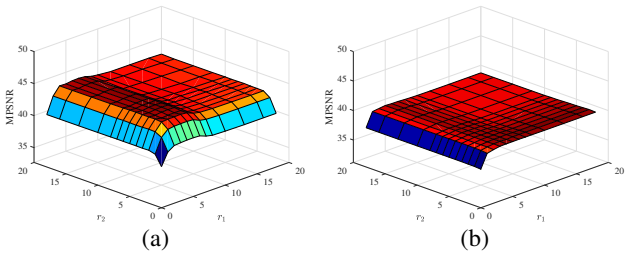

Figure 9. MPSNR change versus r_1 and r_2 on the WDC and PaviaU datasets under Case 4. (a) WDC (with $\beta = 0.9$). (b) PaviaU (with $\beta = 0.8$).

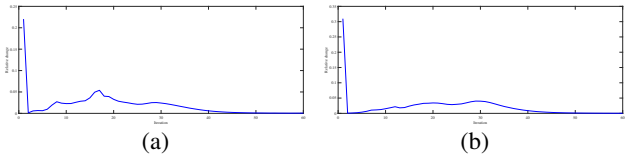

Figure 10. Relative change values of the image component versus the iteration number on the simulated WDC and PaviaU datasets. (a) WDC. (b) PaviaU.

Wang, Y., Peng, J., Zhao, Q., Leung, Y., Zhao, X.-L., Meng, D., 2018. Hyperspectral image restoration via total variation regularized low-rank tensor decomposition. *IEEE J. Sel. Topcis Appl. Earth Observ. Remote Sens.*, 11(4), 1227–1243.

Xu, S., Cao, X., Peng, J., Ke, Q., Ma, C., Meng, D., 2022. Hyperspectral image denoising by asymmetric noise modeling. *IEEE Trans. Geosci. Remote Sens.*, 60. Art. no. 5545214.

Yang, F., Hu, Q., Su, X., 2025. Hyperspectral Image Denoising Based on Hyper-Laplacian Total Variation in Spectral Gradient Domain. *IEEE Trans. Geosci. Remote Sens.*, 63. Art. no. 5507917.

Yao, J., Meng, D., Zhao, Q., Cao, W., Xu, Z., 2019. Nonconvex-sparsity and nonlocal-smoothness-based blind hyperspectral unmixing. *IEEE Trans. Image Process.*, 28(6), 2991–3006.

Yuan, Q., Zhang, L., Shen, H., 2012. Hyperspectral image denoising employing a spectral–spatial adaptive total variation model. *IEEE Trans. Geosci. Remote Sens.*, 50(10), 3660–3677.

Zhang, H., He, W., Zhang, L., Shen, H., Yuan, Q., 2013. Hyperspectral image restoration using low-rank matrix recovery. *IEEE Trans. Geosci. Remote Sens.*, 52(8), 4729–4743.

Zhang, Q., Zheng, Y., Yuan, Q., Song, M., Yu, H., Xiao, Y., 2024. Hyperspectral image denoising: From model-driven, data-driven, to model-data-driven. *IEEE Trans. Neural Netw. Learn. Syst.*, 35(10), 13143–13163.

Zhao, J., Zhong, Y., Shu, H., Zhang, L., 2016. High-resolution image classification integrating spectral-spatial-location cues by conditional random fields. *IEEE Trans. Image Process.*, 25(9), 4033–4045.

Zhou, Y., Chen, Y., Zeng, J., He, W., Huang, M., 2024. Unidirectional Spatial and Spectral Smoothed Tensor Ring Decomposition for Hyperspectral Image Denoising and Destriping. *IEEE Geosci. Remote Sens. Lett.*, 21, 1–5.

Zhuang, L., Ng, M. K., 2023. FastHyMix: Fast and parameter-free hyperspectral image mixed noise removal. *IEEE Trans. Neural Netw. Learn. Syst.*, 34(8), 4702–4716.